Thermally induced interfacial instabilities and pattern formation in confined liquid nanofilms

Hadi Nazaripoor, M. R. Flynn, Charles R. Koch, and Mohtada Sadrzadeh[*]

Department of Mechanical Engineering, 10-367 Donadeo Innovation Center for Engineering, University of Alberta,
Edmonton, Alberta T6G 1H9, Canada

The dynamics, instability, and pattern formation of thermally triggered thin liquid films are investigated numerically under a long-wave limit approximation. To determine the mechanisms responsible for instability growth and pattern formation in confined heated nanofilms, acoustic phonon (AP) and thermocapillary (TC) models are examined using both linear and nonlinear analyses. Under uniform heating conditions, both AP and TC models predict the formation of raised columnar structures (pillars) and bicontinuous structures for very low and high filling ratios defined as the ratio of the initial film thickness to the plate separation distance, D^{-1}. A transition threshold is observed when $D \approx 2.5$. However, the TC model predicts smaller features for larger D, whereas the opposite prediction applies for the AP model. Under spatially variable cooling conditions involving a patterned top plate, both TC and AP models exhibit similar predictions: pillars form under the top plate protrusions. When the heating is spatially variable, the lower plate is patterned; the AP model predicts pillar formation above ridges, whereas the TC model predicts pillar formation above the valleys.

I. INTRODUCTION

Over the past decades there has been a tremendous effort to fabricate micron- and nano-sized features by forming, reforming, and fixing soft matters [1–4]. Surface patterning of semiconducting and conducting polymers (organic or inorganic) and metamaterials is in high demand for various applications in nanoelectronics and nanophotonics. Novel and versatile approaches, with low cost and high throughput that overcome limitations inherent in conventional lithographic techniques, have been developed [4]. Lithographically induced self-assembly is a recent alternative approach that relies on the self-organization and surface instabilities triggered by external forces such as thermal [5,6], mechanical [7], electrical [8–10], intermolecular [11], or their combination [12]. Polymer melt deformation results in three-dimensional (3D) micro- and nano-structures with ultrasmooth surfaces after solidification which are highly desired for optical applications [13].

Thermally induced instabilities in thick films (thickness in the range of hundreds of micrometers to millimeters) are governed by short-wavelength Bénard-Marangoni (SW-BM) instabilities and have been studied over the past century [14]. By contrast, investigations into nanofilms are more recent and started with the initial observation of one-dimensional (1D) ridge and two-dimensional (2D) pillar (raised columnar structure) microarray formation in a molten polymer film which is heated from below and cooled from above [8]. A schematic view of a thin film sandwiched between two plates is presented in Fig. 1.

A surface charge (SC) model provided the first predictions concerning the formation of periodic nanopillar arrays including descriptions their lateral distributions. In this model, the SC present in the molten polymer and the resulting imaged charge on the plates generates an electrostatic force leading to interfacial deformation. Based on a linear stability (LS) analysis, the characteristic wavelength, λ, associated with the maximum growth rate depends on the initial film thickness, plate separation distance, interfacial tension, and electrical properties of the polymer melt such as permittivity and interfacial charge density [8]. Further studies showed that changing the thermal properties of the system and the imposed thermal gradient affects the resulting feature size or λ.

Subsequent theoretical and experimental studies suggested acoustic phonon (AP) as the main mechanism for inducing instabilities. The AP model is based on an internal film pressure induction of low-frequency acoustic phonons in molten polymers [7] and considers the thermal properties of the melted polymer. The role of the imposed temperature gradient in the prediction of the dominant wavelength of the instabilities is considered in the AP model but was not taken into account in the SC model. Hence, the AP model predictions were found to be in better agreement with the experimental results as compared to the SC model. In the AP model, the LS predicted λ depends on the temperature difference, thermal conductivity of molten polymer and bounding layer, speed of sound in the molten polymer, acoustic phonon coefficient, initial film thickness, plate separation distance, and interfacial tension.

More recently, a model developed based on the Bénard-Marangoni (BM) instability in the long-wave (LW) limit and called the thermocapillary (TC) model has been derived [15,16]. The temperature gradient along the air-liquid interface leads to an interfacial tension gradient that exerts a tangential TC stress at the interface. The TC stress disturbs the interface, whereas the Laplace and viscous stresses tend to depress such out-of-plane deformations. In the LW-BM instability, the film deforms due to a growth of the instabilities over

---
[*]sadrzade@ualberta.ca

time. As the thermally induced pattern formation is a transient process, similar to other self-organized pattern formation phenomena [11], the size and shape of the resulting structures highly depend on the time when the system is cooled down to solidify the structures. Controlling the shape and size of the generated features by a self-assembly patterning process is important for practical applications. Different techniques have therefore been applied for this purpose, like using a patterned mask in electrically induced patterning [9,17] and chemically heterogeneous substrates in dewetting induced patterning [11,18].

Complementing the predictions of LS analyses, experimental studies have been performed to try to determine the principal mechanism driving instability growth [19]. Early time measurements showed good agreement between the TC model predictions and laboratory data when the out-of-plane thermal conductivity of the molten polymer was several times larger than that of the bulk, which could, in turn, be attributed to polymer chain alignment [20]. Feature extraction techniques and thermal gradient assessment were later improved [21] to capture the fastest growing wavelength at earlier times and to accurately predict the temperature gradient in the thin film. In spite of these expanded laboratory capabilities, the discrepancy between the theory and experimental results was attributed to experimental challenges such as accurately measuring the temperature difference that the molten polymer film is exposed to.

To date, the majority of the work performed has focused on finding the best theoretical model to describe the formation of micropillar array formation. However, there is still a discrepancy between AP and TC model predictions and complementary experimental observations. Moreover, the AP and TC models exhibit important differences, e.g., the force direction at the interface. In the TC model, the force acts in a tangential direction to the interface whereas in the AP model it acts normal to the interface. This study will employ linear and nonlinear analyses to investigate the similarities dissimilarities between the TC and AP model predictions vis-à-vis dynamics, the spatiotemporal evolution of the nanofilms, and the size and shape of the resulting features. In most previous studies, the polymer film is exposed to a uniform temperature gradient. In this work, we also extend the thermally induced patterning to nonuniform heating and cooling conditions using patterned top and bottom plates.

II. MATHEMATICAL MODEL

A. Governing equations

A schematic of the ultrathin liquid film confined between two parallel palates is shown in Fig. 1. The liquid film is heated from below (T_H) to above the glass transition temperature of the polymer (T_g) and cooled from above (T_C) so that $T_H - T_C > T_g$. A transverse thermal gradient induces an interfacial thermal pressure (either a tangential TC stress or a normal AP stress). The TC pressure is due to the temperature gradient along the interface and leads to nonuniformity in the interfacial tension. A local increase in the interfacial temperature leads to a lower interfacial tension compared to neighboring cold areas. The hot interface region is thereby
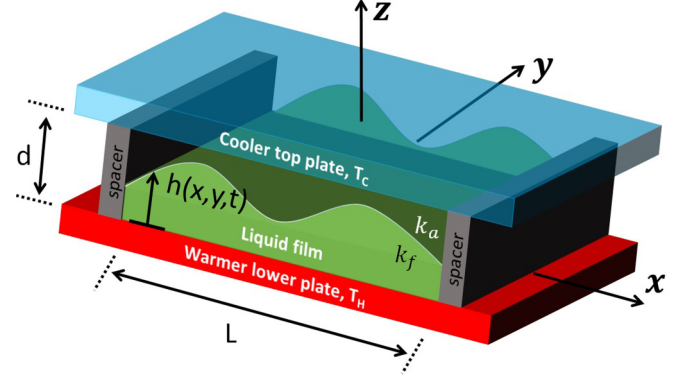

FIG. 1. A 2D schematic of the ultrathin liquid film sandwiched between top (cold) and bottom (hot) plates.

pulled toward colder area leading to the BM instabilities. However, the internal film pressure in the AP model is due to the induction of low-frequency acoustic phonons in the polymer film.

To describe the spatiotemporal evolution of the film under TC stress, we employ mass conservation and momentum and energy balances for an incompressible Newtonian film, which are respectively written as

$$\nabla \cdot \vec{u}_i = 0, \qquad (1)$$

$$\rho_i \left[\frac{\partial \vec{u}_i}{\partial t} + (\vec{u}_i \cdot \nabla \vec{u}_i) \right] = -\nabla P_i + \nabla \cdot \{\mu_i [\nabla \vec{u}_i + (\nabla \vec{u}_i)^T]\}, \qquad (2)$$

$$\rho_i c_{p_i} \left(\frac{\partial T_i}{\partial t} + \vec{u}_i \cdot \nabla T_i \right) = k_i \nabla^2 T. \qquad (3)$$

Subscript i differentiates between the following fluid phases: molten polymer film and air as a bounding layer. In the energy balance equation, energy dissipation due to viscous forces is assumed to be negligible. The film viscosity $\mu = \mu(T_H)$ and density $\rho = \rho(T_H)$ are assumed constant, i.e., the effect of variable viscosity due to thermal gradients and variations in the film thickness [22] is not considered. The thermal conductivity is k_i, heat capacity is c_{p_i}, and fluid velocity is $\vec{u}_i$. The hydrodynamic and thermal boundary conditions are

$$\vec{u}_1 = 0; \quad T_1 = T_H \quad \text{at} \quad z = 0, \qquad (4)$$

$$\vec{u}_2 = 0; \quad T_2 = T_C \quad \text{at} \quad z = d. \qquad (5)$$

At the interface [$z = h(x, y, t)$] the boundary conditions are

$$\vec{u}_{\text{rel}} = 0 \quad \text{and} \quad T_1 = T_2, \qquad (6)$$

thermal conduction: $\quad \vec{n} \cdot (k_1 \nabla T_1 - k_2 \nabla T_2) = 0. \qquad (7)$

Finally, the normal and tangential stress balances are

$$\vec{n} \cdot [\bar{\sigma}_1 \cdot \vec{n} - \bar{\sigma}_2 \cdot \vec{n}] = \kappa \gamma, \qquad (8)$$

$$\vec{t}_j \cdot [\bar{\sigma}_1 \cdot \vec{n} - \bar{\sigma}_2 \cdot \vec{n}] = \nabla_s \gamma \cdot \vec{t}_j, \qquad (9)$$

respectively.

The stress tensor $\bar{\sigma} = -P\bar{I} + \mu_i[\nabla\vec{u}_i + (\nabla\vec{u}_i)^T]$ is defined as the summation of hydrostatic and viscous stresses. For the normal stress balance, the capillary pressure is $\kappa\gamma$ with $\kappa = (\frac{1}{R_1} + \frac{1}{R_2})$ the mean interfacial curvature of the film interface [23] defined as

$$
\frac{1}{R_1} + \frac{1}{R_2}
$$
$$
= \frac{\frac{\partial^2 h}{\partial x^2}[1 + (\partial h/\partial y)^2] + \frac{\partial^2 h}{\partial y^2}[1 + (\partial h/\partial x)^2] - \frac{\partial^2 h}{\partial x \partial y}\frac{\partial h}{\partial x}\frac{\partial h}{\partial y}}{[1 + (\partial h/\partial x)^2 + (\partial h/\partial y)^2]^{\frac{3}{2}}}.
$$
(10)

The term $\nabla_s\gamma = (d\gamma/dT)\nabla_s T|_{z=h}$ is the interfacial tension gradient along the interface, which represents the TC pressure in the tangential stress balance at the interface. The surface tension is assumed to decrease linearly with the interfacial temperature [14], i.e., $\gamma = \gamma_0 - \alpha(T - T_0)$, where α (>0), γ_0, and T_0 are the surface tension gradient, the reference interfacial tension, and the reference temperature, respectively.

The normal $\vec{n}$ and tangential vectors $\vec{t}_j$ ($j = 1, 2$) of the interface [23] are

$$
\vec{n} = \frac{1}{C_n}\left(\frac{\partial h}{\partial x}, \frac{\partial h}{\partial x}, -1\right) \quad \text{and}
$$

$$
C_n = [1 + (\partial h/\partial x)^2 + (\partial h/\partial y)^2]^{\frac{1}{2}},
$$
(11)

$$
\vec{t}_1 = \frac{1}{C_{t1}}\left(-\frac{\partial h}{\partial y}, \frac{\partial h}{\partial x}, 0\right) \text{ and } C_{t1} = [(\partial h/\partial x)^2 + (\partial h/\partial y)^2]^{\frac{1}{2}},
$$
(12)

$$
\vec{t}_2 = \frac{1}{C_{t2}}\left[\frac{\partial h}{\partial x}, \frac{\partial h}{\partial y}, \left(\frac{\partial h}{\partial x}\right)^2 + \left(\frac{\partial h}{\partial y}\right)^2\right], \quad \text{and}
$$

$$
C_{t1} = \left\{(\partial h/\partial x)^2 + (\partial h/\partial y)^2 + \left[\left(\frac{\partial h}{\partial x}\right)^2 + \left(\frac{\partial h}{\partial y}\right)^2\right]^2\right\}^{\frac{1}{2}}.
$$
(13)

Finally, to relate the interface height to the interfacial velocity components, a kinematic boundary condition [24] is imposed:

$$
w = \frac{\partial h}{\partial t} + u\frac{\partial h}{\partial x} + v\frac{\partial h}{\partial y} \quad \text{at} \quad z = h(x, y, t).
$$
(14)

B. Dynamics of the film: The long-wave approximation

The governing equations [Eqs. (1)–(3)] and boundary conditions [Eqs. (4)–(9)] are normalized using the initial film thickness, h_0, for the vertical coordinate, interface height, and electrodes distance ($Z = z/h_0$, $H = h/h_0$, and $D = d/h_0$) and characteristic wavelength for the growth of instabilities, L, for the lateral coordinates ($X, Y = x/L, y/L$). The normalized velocity and time are defined, respectively, as $\vec{U} = (u/u_c, v/u_c, w/\epsilon u_c)$ and $\tau = (u_c/L)t$. Here $\epsilon = h_0/L$ is the slender gap ratio defined as the ratio of initial film thickness to the lateral length scale and u_c is the characteristic lateral

velocity due to the TC-induced flow. The normalized pressure is defined as $P = (p + \phi)/(\mu u_c/\epsilon h_0)$ in which p accounts for capillary pressure, and $\phi = -\rho gz + \phi_{LW}$ incorporates the hydrostatic pressure and intermolecular interactions. Lifshitz-van der Waals interactions, $\phi_{LW} = -A/(6\pi h^3)$, are considered here as the film thickness is in the submicron range [25]. The effective Hamaker constant, A, is found for the three-layer system (substrate-film-air). The normalized temperature is defined as $\Theta = (T - T_C)/\Delta T$ where $\Delta T = T_H - T_C$ is the maximum temperature difference.

In this study, because the bounding layer is considered to be air ($\mu_2/\mu_1 \ll 1$ and $\rho_2/\rho_1 \ll 1$), the hydrodynamics of the polymer film are unaffected by this overlying air layer. Nonetheless, the two sets of governing equations (polymer film and air) are coupled at the interface by stress balances. The flow induced by TC tangential stresses is considered a creeping flow since the Reynolds number, $\text{Re} = \rho u_c h_0/\mu$, is less than unity. Using the scaling factors and employing the long-wave approximation ($\epsilon, \epsilon^2 \ll 1$), the simplified governing equations are

$$
\frac{\partial U}{\partial X} + \frac{\partial V}{\partial Y} + \frac{\partial W}{\partial Z} = 0,
$$
(15)

$$
\frac{\partial^2 U}{\partial Z^2} = \frac{\partial P}{\partial X}, \quad \frac{\partial^2 V}{\partial Z^2} = \frac{\partial P}{\partial Y}, \quad \frac{\partial P}{\partial Z} = 0,
$$
(16)

$$
\frac{\partial^2 \Theta}{\partial Z^2} = 0.
$$
(17)

The corresponding boundary conditions, on the walls are

$$
\vec{U}_1 = 0; \quad \Theta = 1 \quad \text{at} \quad Z = 0,
$$
(18)

$$
\Theta = 0 \quad \text{at} \quad Z = D,
$$
(19)

and at the interface $[Z = H(X, Y, \tau)]$ are

$$
\vec{U}_{\text{rel}} = \vec{0} \quad \text{and} \quad \Theta_1 = \Theta_2,
$$
(20)

thermal conduction: $k_1 d\Theta_1/dZ - k_2 d\Theta_2/dZ = 0$. (21)

The stress balances are

$$
P = -\text{Ca}^{-1}\nabla^2 H + \text{Ca}^{-1}\text{Bo}H + \overline{A}H^{-3},
$$
(22)

$$
\frac{\partial U}{\partial Z} = \frac{\partial \Gamma}{\partial X}, \quad \frac{\partial V}{\partial Z} = \frac{\partial \Gamma}{\partial Y},
$$
(23)

where $\text{Ca} = \mu u_c/(\epsilon^3\gamma)$ is the capillary number and $\text{Bo} = \rho g L^2/\gamma$ is the Bond number. The last term on the right-hand side of Eq. (22) accounts for Lifshitz-van der Waals pressures in which $\overline{A}$ is a dimensionless Hamaker constant defined as $\overline{A} = \frac{A/(6\pi)}{(\mu u_c/\epsilon h_0)}$. The term $\Gamma = \gamma/(\mu u_c/\epsilon)$ is the dimensionless interfacial tension and, its gradient at the interface is related to the temperature gradient as

$$
\nabla_s\Gamma = -\text{Ma}\nabla\Theta|_{Z=H},
$$
(24)

where $\text{Ma} = \epsilon\alpha\Delta T/(\mu u_c)$ is the Marangoni number. The temperature distribution along the interface is given by $\Theta|_{Z=H} = k_r(D - H)/[(1 - k_r)H + k_r D]$ in which $k_r = k_1/k_2$ is the relative thermal conductivity of the lower and

upper layers. Substituting the temperature distribution into Eq. (24) yields

$$\nabla_s \Gamma = \frac{\text{Ma}\, k_r D}{[(1-k_r)H + k_r D]^2} \nabla H. \quad (25)$$

The characteristic lateral velocity, $u_c = \epsilon \alpha k_r D \Delta T / \{\mu[k_r(D-1)+1]^2\}$ and Marangoni number, $\text{Ma} = [(1-k_r)+k_r D]^2/(k_r D)$, are found when the film thickness H, interfacial slope ∇H, and TC stress $\partial \Gamma/\partial X = \partial U/\partial Z$ in Eq. (25) are on the order of unity and are set to one.

Finding the in-plane velocity components using Eqs. (15)–(23) and then substituting into the kinematic boundary condition relation

$$W = \frac{\partial H}{\partial \tau} + U \frac{\partial H}{\partial X} + V \frac{\partial H}{\partial Y} \quad (26)$$

results in the following dimensionless equation, which describes the spatiotemporal evolution of thin liquid film subjected to the transverse thermal gradient. The contribution of gravity is neglected as it is negligible because the film thickness is on the order of submicrons:

$$\frac{\partial H}{\partial \tau} + \nabla \cdot \left\{ \frac{H^3}{3}[\text{Ca}^{-1}\nabla(\nabla^2 H) + \overline{A} H^{-2}\nabla H] \right.$$
$$\left. + \frac{H^2}{2}\frac{\text{Ma}\, k_r D}{[(1-k_r)H + k_r D]^2}\nabla H \right\} = 0. \quad (27)$$

In the AP model [26–28], an acoustic radiation pressure acts on the interface due to the different acoustic impedances of air and molten polymer. The radiation pressure, ϕ_{AP}, depends on the thermal energy flux (J_q), reflectivity coefficient (Q), and speed of sound in the polymer (u_p):

$$\phi_{\text{AP}} = -\frac{2Q J_q}{u_p}. \quad (28)$$

The reflectivity coefficient is a material property incorporating all three phases in the system (air, polymer melt, and the solid bounding plates). Here the value $Q = 6.2$ is adopted, which is appropriate to the case of an air-polystyrene double layer sandwiched between silicon wafers. More details about the calculation of Q are available in the literature [26–28]. The direction of the energy flux J_q is from high to low temperatures; the magnitude depends on the thermal conductivity of each layer in the system. More precisely,

$$J_q = \frac{k_1 \Delta T}{(1-k_r)h + k_r d}. \quad (29)$$

To find the spatiotemporal evolution of interface using the AP model, the thin film equation is rederived starting from the governing equations and boundary conditions presented above [Eqs. (1)–(14)]. The TC tangential stress ($\nabla \Gamma$) is set to zero. To keep the Laplace pressure in the long-wave limit ($\epsilon \ll 1$), Ca is set to unity, which results in the characteristic velocity being defined as $u_c = \gamma \epsilon^3/\mu$. The radiation pressure defined in Eq. (28) is normalized as $\Phi_{\text{AP}} = \phi_{\text{AP}}/(\mu u_c/\epsilon h_0)$. This term is added to the pressure defined by Eq. (22).

The resulting nondimensional thin film equation for the AP case reads

$$\frac{\partial H}{\partial \tau} + \nabla \cdot \left\{ \frac{H^3}{3}\left[\text{Ca}^{-1}\nabla(\nabla^2 H) + \overline{A} H^{-2}\nabla H \right. \right.$$
$$\left. \left. + 8\pi^2 \frac{\text{Ma}\, k_r D}{[(1-k_r)H + k_r D]^2}\nabla H \right] \right\} = 0. \quad (30)$$

Interestingly, in the normalized form presented above, the AP force is similar to the TC force shown in Eq. (25) with an extra coefficient of $8\pi^2$. However, the AP force acts normal to the interface whereas the TC force acts tangentially.

C. Linear stability analysis

To find the lateral scaling factors of L, a linear stability (LS) analysis is used to predict the maximum and characteristic wavelength of the TC instabilities. The uniform interface height, H in Eq. (27), is superposed with a periodic perturbation such that $H = 1 + \xi \exp[\overline{\kappa}(X+Y)\text{i} + S(\overline{\kappa})\tau] + \text{c.c.}$ where $\text{i} = \sqrt{-1}$ and c.c. denotes the complex conjugate. To satisfy the linear deformation, the perturbation amplitude is set to be small, $\xi \ll 1$. The wave number $\overline{\kappa}$ corresponds to the wavelength ($\lambda = 2\pi L/\overline{\kappa}$) and the growth rate [$S(\overline{\kappa})$]. After expanding Eq. (27) for this small perturbation and neglecting all resulting nonlinear terms, the following dispersion relation is obtained (see the Appendix for more details):

$$S(\overline{\kappa}) = -\overline{\kappa}^2 \left\{ \frac{\overline{\kappa}^2}{\text{Ca}} - \frac{3\text{Ma}\, k_r D}{2[(1-k_r)+k_r D]^2} \right\}. \quad (31)$$

Zeros of this dispersion relation $S(\overline{\kappa}_0) = 0$ indicate the disturbances, which remain unchanged over time. The film remains stable if $S(\overline{\kappa}) < 0$ such that the disturbances are damped over time. In the absence of any hydrostatic stabilizing force, the TC-induced instabilities in confined nanofilms always lead to pattern formation as there is always a wave number band, $0 < \overline{\kappa} < \overline{\kappa}_0 = \sqrt{3\text{Ca}\,\text{Ma}\, k_r D/2[(1-k_r)+k_r D]^2}$, where $S(\overline{\kappa}) > 0$. This is in contrast with the TC instabilities in thicker films where disturbances in the system are amplified only if a certain criterion given by critical Ma is met [29]. The fastest growing wave corresponding to the dominant wave number corresponds to the positive root of $\partial S/\partial \overline{\kappa} = 0$. Evaluating the derivative in question yields

$$\lambda_{\text{max}} = 2\pi L \sqrt{\frac{4[1 + k_r(D-1)]^2}{3\text{Ca}\,\text{Ma}\, k_r D}}. \quad (32)$$

By substituting Ca and Ma in Eq. (32), λ_{max} can be rewritten as

$$\lambda_{\text{max}} = 2\pi [h_0(1-k_r) + k_r d] \sqrt{\frac{4\gamma h_0}{3d\alpha k_r \Delta T}}. \quad (33)$$

By contrast, λ_{max} for the AP model is given by

$$\lambda_{\text{max}} = 2\pi [h_0(1-k_r) + k_r d] \sqrt{\frac{\gamma u_p}{Q k_1 (k_r - 1)\Delta T}}. \quad (34)$$

The above result was obtained using a similar kind of LS analysis as outlined above [27,28]. A list of all dimensionless parameters and their values for the cases considered in this study is presented in Table I.

TABLE I. List of dimensionless numbers and their values.

Dimensionless number	Definition	Value
Interface height (H)	$h(x, y, t)/h_0$	0.02–8.00
Marangoni number (Ma)	$[(1 - k_r) + k_r D]^2/k_r D$	1.56–14.54
Capillary number (Ca)	$\mu u_c/(\epsilon^3 \gamma)$	1.00–52.67
Bond number (Bo)	$\rho g L^2/\gamma$	10^{-8}–10^{-6}
Inverse of filling ratio (D)	d/h_0	1.5–4.0
Slender gap ratio (ϵ)	h_0/λ_{max}	0.1–0.01

TABLE II. Constants and parameters used in simulations.

Parameter	Value
Interfacial tension (γ)	0.045 N/m
Interfacial tension gradient (α)	88.5×10^{-5} N/m °C
Viscosity of liquid film (μ)	1 Pa s
Thermal conductivity of liquid film (k_1)	0.13 W/m °C
Thermal conductivity of air (k_2)	0.036 W/m °C
Effective Hamaker constant (A)	-1.5×10^{-21} J
Mean initial film thickness (h_0)	20–70 nm
Plate separation distance (d)	80–100 nm
Equilibrium distance (l_0)	1 nm
Temperature difference (ΔT)	46 °C
Speed of sound in the polymer [28] (u_p)	1850 m/s
Grid points (n_x, n_y)	121–171

D. Numerical modeling

To derive insights into the dynamics, instability, and morphological evolution of the nanofilm over and above what can be realized from an LS analysis, we solve the nonlinear thin film equation, which is a fourth-order nonlinear partial differential equation (PDE). Applying the finite difference (FD) discretization and using a second-order central finite difference scheme to the spatial derivatives ($\partial/\partial X$ and $\partial/\partial Y$) results in a system of ordinary differential equations (ODEs) in time:

$$F(\tau, H, \partial H/\partial \tau) = 0, \tag{35}$$

where F, H, and $\partial H/\partial \tau$ are vectors whose lengths are related to the dimension of the spatial grid.

In order to solve the resulting sets of ODEs, an adaptive time step ODE solver of DASSL (in the SLATEC library [30]) is employed [31–34]. In the DASSL algorithm, the time derivative is replaced by a higher order (i.e., kth-order with k ranging from one to five) backward difference formula (BDF). DASSL accepts the fixed time steps as an input whereas it chooses the interval time step size and order of k based on the behavior of the solution. In this way, the scheme is called an adaptive time step solver. In the current study, and to improve the efficiency and reduce the computation time, the input time intervals are also set as adaptive; these are updated based on the last successful time interval of DASSL. Because the thin film equation is a nonlinear PDE that requires different time steps depending on the stage of thin film evolution, using an adaptive time step significantly reduces computational demands. Further details about the numerical scheme are available in Ref. [35]. Numerical runs are performed in a square domain having periodic boundary conditions and a length of $9\lambda_{max}$ or $10\lambda_{max}$. This domain is large enough to enable instabilities to grow and saturate [18]. The film thickness is initialized using random perturbations about the predetermined mean value.

The majority of laboratory experiments to date have either used polymers like polystyrene (PS) [7,15,16,19,21,27,28] with a smaller number of investigations employing poly(methyl methacrylate) (PMMA) [8]. As such, we consider in this study constants and parameters derived from the reported properties of PS polymer [21]; see Tables I and II. Meanwhile, the temperature difference applied across the liquid polymer film is 46°C, which falls within the range (10°C to 55°C) considered in complementary investigations [7,15,16,19,21,27,28].

III. RESULTS AND DISCUSSION

A. Uniformly heated nanofilms: TC model

As a baseline, first the spatiotemporal evolution of a uniformly heated nanofilm examined. The interface height profile and corresponding 3D snapshots for a 25 nm thick film are presented in Fig. 2. Initial random perturbations redistributed at the early stages of pattern formation and the resulting bicontinuous structures including sets of ridges and valleys are shown in Fig. 2(a). Based on the TC pressure relation [Eq. (25)], a higher TC force is applied to the thicker regions compared to the thinner regions. Hence, peaks get pushed upwards toward the top cold plate, which has the effect of depleting fluid from adjoining valley, which are, in turn, pushed downwards. This fluid flow from thinner to thicker regions in a film is called negative diffusion [18]. Next, fragmentation occurred on the ridges and separate islands form. The inward fluid flow from the surroundings into the thicker regions leads to the formation of raised columnar structures, called pillars, which bridge the two confining plates [Fig. 2(b) and Fig. 2(c)]. The so-formed pillars are randomly distributed over the domain area, and their number increases as a function of time.
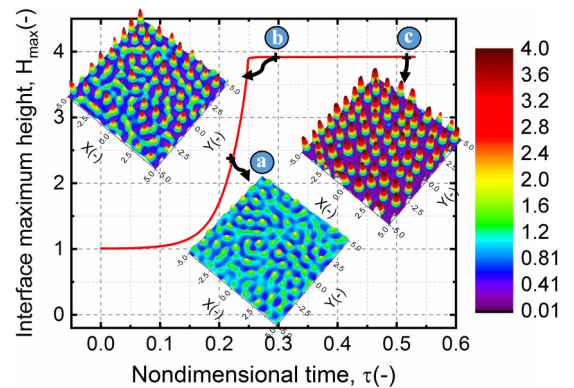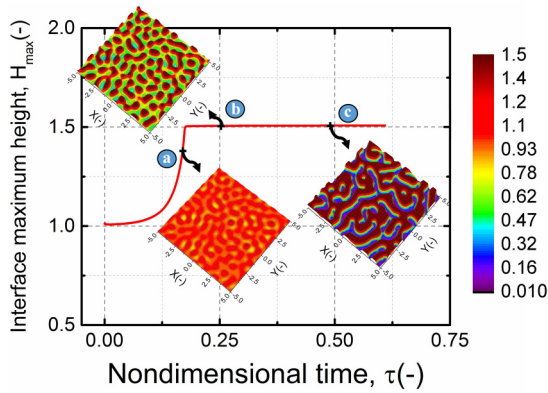

FIG. 2. TC model, interface height profile versus time, and the 3D snapshots of the interface. Initial film thickness, $h_0 = 25$ nm, plate separation distance, $d = 100$ nm, temperature difference, $\Delta T = 46$ °C, and nondimensional times, $\tau =$ (a) 0.225, (b) 0.306, and (c) 0.528.

FIG. 3. TC mode, interface height profile versus time, and the 3D snapshots of the interface. Initial film thickness, $h_0 = 55$ nm, plate separation distance, $d = 100$ nm, temperature difference, $\Delta T = 46\,^{\circ}$C and nondimensional times, $\tau = $ (a) 0.17, (b) 0.252 and (c) 0.49.

The LS analysis showed that the characteristic wavelength decreases in both the TC and AP models when we consider thicker polymer films or, equivalently, larger values for $D^{-1} = h_0/d$. Thicker films therefore lead to the formation of structures with smaller lateral dimensions (higher spatial resolution), which is of interest for many practical applications like semiconductor fabrication. Hence, the initial film thickness of film was increased from 25 nm to 65 nm while the plate separation distance was kept constant at 100 nm. The spatiotemporal evolution of the interface in this latter numerical simulation is investigated in Fig. 3, and here

qualitatively different behavior is noted as compared to that exhibited in Fig. 2. At the initial stages, the random disturbances form bicontinuous structures in a manner similar to the case involving thinner films [shown in Fig. 2(a)]. However, the film interface at the ridges reached the top cold plate early on, which inhibits a complete fragmentation of the ridges and gives rise to the cellular pattern exhibited in Fig. 3(c) at later times.

A further difference between Figs. 2 and 3 is that the coarsening mechanism in the latter case, i.e., the collision of neighboring pillars and the Oswalt ripening happened simultaneously during the early stages of pattern formation. This blending of pillar collision and Oswalt ripening leads to the formation of bicontinuous structures as shown in Fig. 3(c). In thinner films structure coarsening proceeds through two sequential stages. At the early stages of coarsening, neighboring pillars of approximately equal size collide and merge to form larger structures (called the collision stage). At later times, the smaller pillars merge to bigger ones (those formed from earlier collisions) to form more stable structures with less surface area [36]. This stage of coarsening is similar to the Ostwald ripening mechanism for the coalescence of neighboring drops or the merging of smaller particles into a larger one. Pillar merger leads to a coarse structure, which is undesirable for the formation of well-ordered structures.

The prediction of pattern type, in particular anticipating whether ridges or pillars will form, was already established in the literature based on the ratio of the plate separation distance to the initial film thickness [28]. The fill ratio threshold for the transition from ridges (bicontinuous structure) to pillars
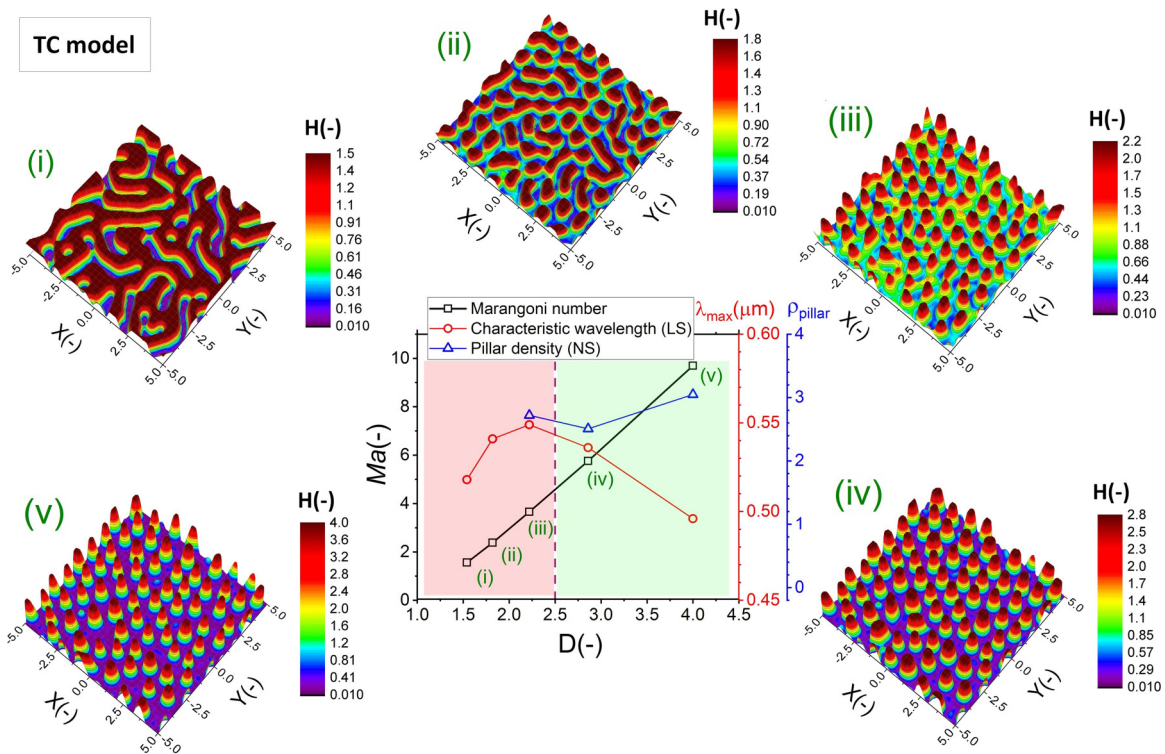

FIG. 4. TC model, (i–v) 3D snapshots of the interface profile. Initial film thickness, $h_0 = $ (i) 65 nm, (ii) 55 nm, (iii) 45 nm, (iv) 35 nm, and (v) 25 nm. Ma = (i) 1.56, (ii) 2.31, (iii) 3.64, (iv) 5.73, and (v) 9.69. Plates distance, $d = 100$ nm, temperature difference, $\Delta T = 46\,^{\circ}$C, and nondimensional times, $\tau = $ (i) 0.49, (ii) 0.30, (iii) 0.26, (iv) 0.41, and (v) 0.53.
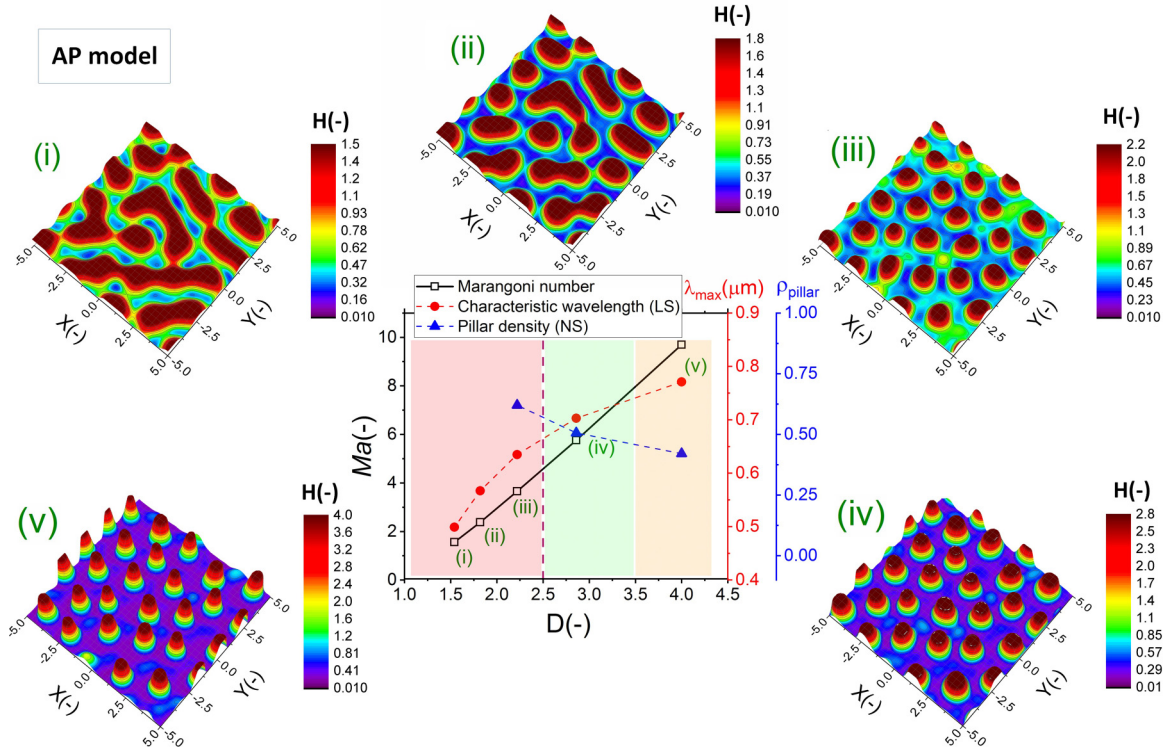
FIG. 5. AP model, (i–vi) 3D snapshots of the interface profile. Initial film thickness, $h_0 =$, (i) 65 nm, (ii) 55 nm, (iii) 45 nm, (iv) 35 nm, (v) 25 nm, and (vi) 25 nm. Plates distance, $d = 100$ nm, temperature difference, $\Delta T = 46\,^{\circ}\mathrm{C}$ and nondimensional times, $\tau =$ (i) 0.10, (ii) 0.10, (iii) 0.07, (iv) 0.10, and (v) 0.10.

was found to be $D \equiv d/h_0 = 3.66$. However, as shown in Figs. 2 and 3, pattern formation is a transient process and shape and size of patterns changes with t. The time required for a particular pattern to form depends on the viscosity of the polymer melt. This transient nature of the patterning process is not considered in the proposed threshold value [28]. Therefore to find the transition threshold from pillar to bicontinuous structure, a nonlinear analysis of pattern formation was performed for different sets of D using both the TC and AP models.

Three-dimensional snapshots of the interface at the quasisteady stage of pattern formation using the TC model for different filling ratios are compared in Figs. 4(i)–4(v). The pattern morphology changes from bicontinuous structures [Fig. 4(i)] to pillars [Fig. 4(v)] as the thickness of the film decreases. For the initially thicker films (small D), the pillars are tightly packed, which increases the collision frequency and the merging of neighboring pillars. Thus, using relatively thinner films is recommended regardless of the size of formed structures. The 2D plot shows the variation of Ma, which represents the relative strength of the TC force to the viscous force for different initial film thicknesses. A linear variation of Ma with D was observed. The characteristic wavelength associated with the most unstable mode from the LS analysis ($\lambda_{\max}$) increased sharply for small D then reached a maximum at $D \simeq 2.25$. Thereafter $\lambda_{\max}$ decreases as the plate separation distance increases. Based on the $\lambda_{\max}$ values predicted by the LS analysis, either using very thick (small D) or very thin (large D) films leads to patterns having finer features. However, the nonlinear simulations showed that only when

starting with thinner films do the desired columnar structures materialize. The final (blue) curve from the 2D plot of Fig. 4 shows the pillar density factor, ρ_{pillar}, defined as the number of pillars formed in a $1\,\mu\mathrm{m}^2$ area and estimated from the numerical simulation output at the quasisteady stage. Thus ρ_{pillar} is a proxy for the compactness of the structures formed as a result of the saturation of the interfacial instability. When D is small [cases (i) and (ii)], only bicontinuous structures formed; ρ_{pillar} cannot then be defined. Although increasing D results in (well-defined) pillars that are more stable and for which $\lambda_{\max}$ is comparatively small, the change of ρ_{pillar} is insignificant. In patterning, both the size and stability (less coarsening effect) of the formed features are vital. Based on the nonlinear simulation results and using the TC model, systems with $D > 2.5$ [cases (iv) and (v)] have a greater likelihood of producing stable and smaller features (green colored area). Next, comparable sets of film thickness and plate separation distances were used to investigate the nonlinear AP model predictions vis-à-vis film dynamics and interface morphology.

B. Uniformly heated nanofilms: AP model

Similar to the TC model, the AP model predicts the formation of bicontinuous structures for thicker films and pillars for smaller filling ratios [Figs. 5(i)–5(v)]. However, the LS analysis for the AP model predicts different trends for $\lambda_{\max}$ in that $\lambda_{\max}$ continuously increased with D. Although, lowering the filling ratio results in stable hexagonally packed pillars with uniform circular cross section, the size of these pillars
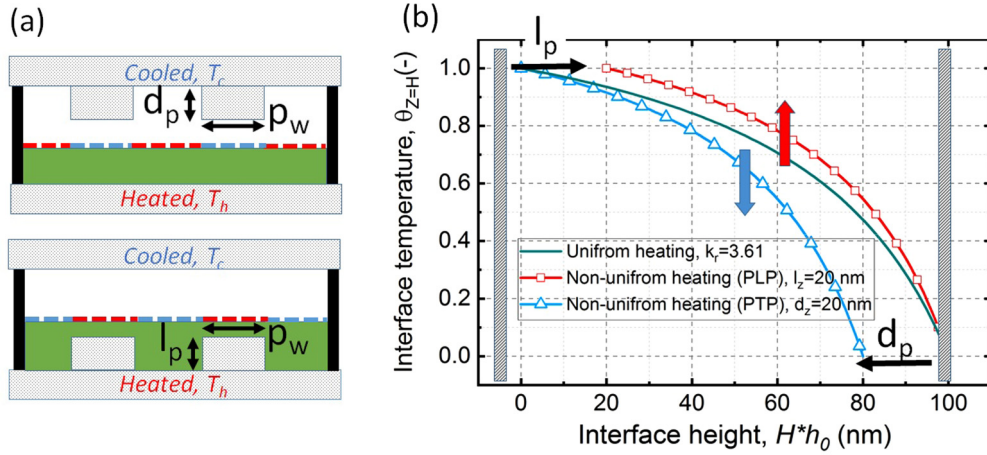
FIG. 6. (a) 2D schematic view of patterned top plate (PTP) and patterned lower plate (PLP) setup. (b) Temperature distribution versus interface height for flat, PTP and PLP configurations. (b) $k_r = 3.61$, $d = 100$ nm, $d_p = l_p = 20$ nm.

increases. Tracking the number of pillars forming in a $1\,\mu m^2$ square domain showed a decline from thicker to thinner films, which is mainly due to a change in λ_{max} as the number of pillars does not changed considerably [cf. cases (iv) and (v)].

The pillars formed in thicker films [cases (i) and (ii)] are highly unstable and merge at the early stages of pattern formation. For thinner films [large D, i.e., cases (iv) and (v)], however, stable pillars were formed. Case (iii) was considered as intermediate: the pillars have oval cross section and are highly unstable. The 3D snapshot images of Fig. 5 show that the number of pillars did not change considerably for cases (iii) to (v). However, the pillar density factor was nontrivially decreased due to an increase in λ_{max}. In the AP model, the D spectrum has three ranges where (1) either bicontinuous structures or pillars are unstable (red region), (2) pillars are stable (green region), or (3) pillars are stable but are larger in size and therefore smaller in pillar density (amber region).

Comparing the values for the pillar density in the TC model ($\rho_{pillar} \geqslant 1$) and the AP model ($\rho_{pillar} < 1$) reveals formation of more compact structures when TC nonlinear waves were considered as the responsible mechanism for the growth of instabilities in heated nanofilms. Regarding the morphology of the interface, both AP and TC models predicted a transition from pillar to bicontinuous structures. The threshold value for this transition ($D \approx 2.5$) should be considered in the context of the time when system is cooled down to freeze the features. Up to this point the TC and AP models have been evaluated from the perspective of uniformly heated conditions. Next, model predictions for nonuniform heated conditions using patterned top plates were examined.

C. Nonuniformly heated nanofilms

In this study we used two methods to impose nonuniform thermal gradients on the interface. The first method consists of using a patterned top plate (PTP), and the second method consists of using a patterned lower plate (PLP). The protrusion height in the PTP configuration is $d_z \neq 0$ and for PLP is $l_p \neq 0$. A 2D schematic view contrasting PTP and PLP is shown in Fig. 6(a). The interfacial temperature versus the interface height is compared between the uniformly heated

film and the PTP and PLP cases in Fig. 6(b). As the film is heated from below and cooled from the top, an increase in the film thickness leads to a lower temperature at the interface. In PTP, addition of descending protrusions of height d_p results in a shift towards lower interfacial temperatures because the cooling is brought in closer proximity to the film. For exactly the same reason, addition of ascending protrusions in the PLP scenario results in higher temperatures at the interface, particularly in interfacial regions immediately above the protruded areas. These two configurations, PTP and PLP, act differently in terms of the temperature nonuniformity applied to the interface.

1. Nonuniform cooling, patterned top plate (PTP)

To investigate the effect of nonuniform heating on the spatiotemporal evolution of thin films, the flat top plate replaced with the patterned plate of Fig. 6(a). The plate separation distance, d, and the protrusion depth, d_p, are 100 nm and 10 nm, respectively. The protrusion width (or width of the ridge) is set to (i) $p_w = \lambda_{max}$ and (ii) $p_w = 0.5\lambda_{max}$ where λ_{max} is the characteristic wavelength predicted by the LS analysis for either the TC model [Eq. (33)] or the AP model [Eq. (34)]. Two-dimensional interface height profiles at early times and analog 3D snapshots at later times are presented for the TC model in Fig. 7. Based on the temperature distribution along the interface, the interfacial tension is higher under the protrusions due to the reduced temperature. Hence, areas with higher interfacial tensions pull areas with lower interfacial tension leading to interfacial deformations. The growth of instabilities at the interface and their subsequent amplification under the protrusions is shown in Fig. 7(a)(i). For the case of $p_w = \lambda_{max}$, two sets of undulations formed under each protrusion reminiscent of a period doubling-type instability. Over time, the undulations in question got larger and bridged the upper and lower plates. At quasisteady state [Fig. 7(b)(i)], a pair of pillars separated by a small gap formed under each protrusion. Lowering (i) $p_w = \lambda_{max}$ to (ii) $0.5\lambda_{max}$ resulted in only one undulation forming under each protrusion. The instability pattern is here better organized and has a lower likelihood of eventual pillar merger.
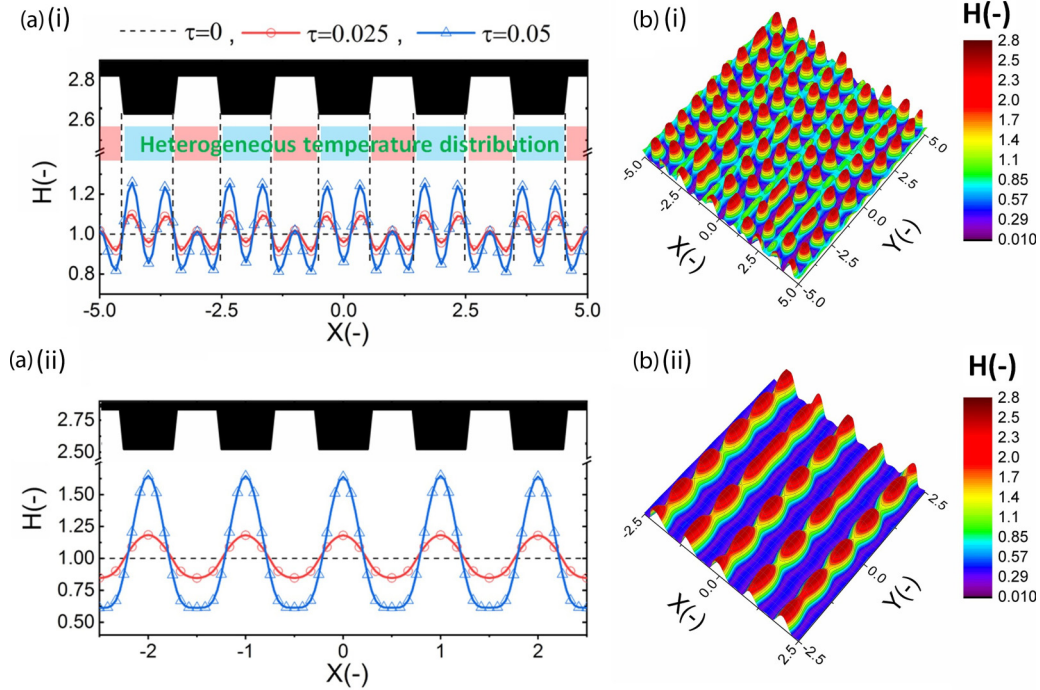
FIG. 7. Patterned top plate (PTP) and TC model, interface height profile at (a) early stages of deformation and (b) quasisteady stage of pattern formation. Protrusion height $d_p = 0.1d$ and protrusion width $p_w = $ (i) λ_{max} and (ii) $0.5\lambda_{max}$, initial film thickness, $h_0 = 35$ nm, and plates distance, $d = 100$ nm.

Similarly the PTP was examined in the AP model to investigate the dynamics and interface evolution at early and late times (see Fig. 8). In the case with $p_w = \lambda_{max}$, and for small t, the interface pulled toward the top cold plate with

two spikes near the edges, which coincided with the largest thermal gradient [Fig. 8(a)(i)]. In later stages, the initially formed peaks merged and exhibited only one undulation under the ridge. At the quasisteady stage, arrays of pillars formed
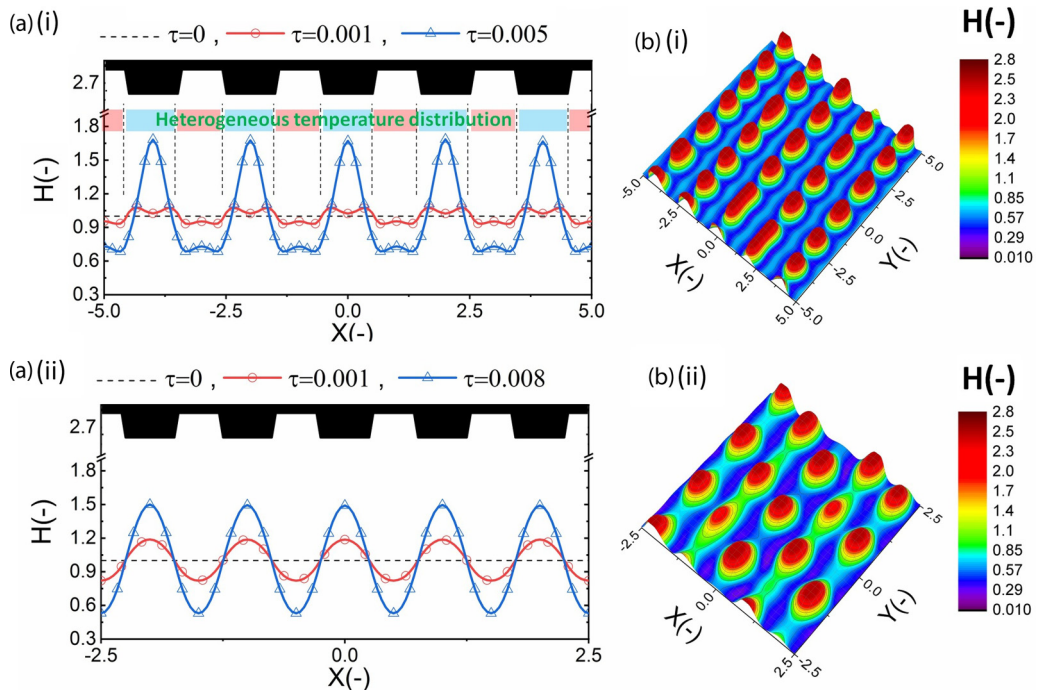

FIG. 8. Patterned top plate (PTP) and AP model, interface height profile at (a) early stages of deformation and (b) quasisteady stage of pattern formation. Protrusion height $d_p = 0.1d$ and protrusion width $p_w = $ (i) λ_{max} and (ii) $0.5\lambda_{max}$, initial film thickness, $h_0 = 35$ nm, and plates distance, $d = 100$ nm.
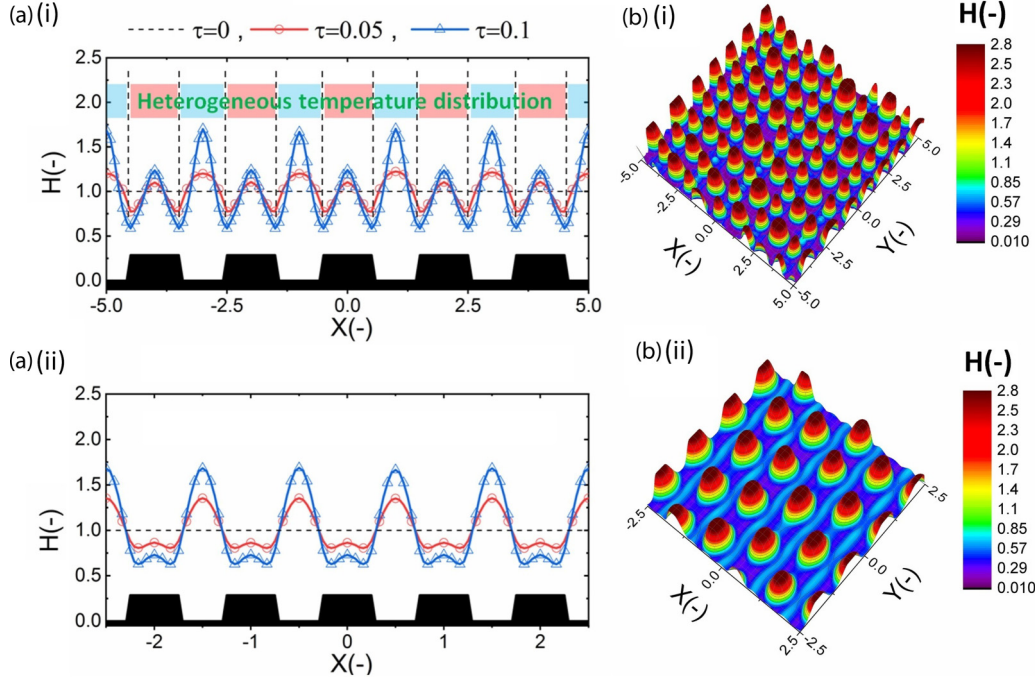
FIG. 9. Patterned lower plate (PLP) and TC model, interface height profile at (a) early stages of deformation and (b) quasisteady stage of pattern formation. Protrusion height $l_p = 0.1d$, and protrusion width $p_w = $ (i) $\lambda_{\max}$ and (ii) $0.5\lambda_{\max}$, initial film thickness, $h_0 = 35$ nm, and plates distance, $d = 100$ nm.

under each ridge as shown in Fig. 8(b)(i). Lowering the protrusion width and the center-to-center distance to $0.5\lambda_{\max}$ [Figs. 8(a)(ii) and 8(b)(ii)], resulted in similar stages of pattern formation as with the $p_w = \lambda_{\max}$ case albeit with smaller pillars in the end.

So far, both the TC and AP models have followed similar trends in interfacial deformation using the PTP configuration, i.e., the interface is pulled toward the top (cold) plate under the protruded areas. However, in the TC model using the predicted $\lambda_{\max}$ for the width of ridges resulted in two arrays of pillars under each ridge, whereas in the AP model only

one array of pillars formed. Next, the effect of using a PLP in introducing temperature nonuniformity in both the TC and AP models will be investigated.

2. Nonuniform heating, patterned lower plate (PLP)

In order to find the the spatiotemporal evolution of the polymer film using a PLP, the thin film equation was rederived by introducing the lower plate protrusion shape function $l_p = f(x, y)$ into the thin film equation by defining $h = h - l_p$. With this modification, the governing Eq. (27) for the TC model becomes

$$\frac{\partial H}{\partial \tau} + \nabla \cdot \left(\frac{(H - L_p)^3}{3} \left\{ \mathrm{Ca}^{-1} \nabla[\nabla^2(H - L_p)] + \overline{A}(H - L_p)^{-2} \nabla(H - L_p) \right\} \right)$$

$$+ \nabla \cdot \left(\frac{(H - L_p)^2}{2} \left\{ \mathrm{Ma}\, k_r \frac{[(D - H)\nabla L_p + (L_p - D)\nabla H]}{[(1 - k_r)H + k_r D - L_p]^2} \right\} \right) = 0. \tag{36}$$

Meanwhile, the equation corresponding to (30) for the AP model is given by

$$\frac{\partial H}{\partial \tau} + \nabla \cdot \left(\frac{(H - L_p)^3}{3} \left\{ \mathrm{Ca}^{-1} \nabla[\nabla^2(H - L_p)] + \overline{A}(H - L_p)^{-2} \nabla(H - L_p) \right\} \right)$$

$$+ \nabla \cdot \left(\frac{(H - L_p)^3}{3} \left\{ 8\pi^2 \frac{\mathrm{Ma}\, k_r [(D - H)\nabla L_p + (L_p - D)\nabla H]}{[(1 - k_r)H + k_r D - L_p]^2} \right\} \right) = 0, \tag{37}$$

where $L_p = \frac{f(x, y)}{h_0}$ is the normalized protrusion height. Equations (36) and (37) are valid for any shape functions of $f(x, y)$. To be consistent with our previous analysis consisting of the nonuniform cooling using a PTP, the same steplike ridge pattern was used for the nonuniform heating

condition using a PLP. The new sets of governing equations were solved under the same geometrical conditions and results for the TC model using a PLP are shown in Fig. 9. This figure confirms that the interface temperature is higher above the protrusions leading to lower interfacial tension compared to
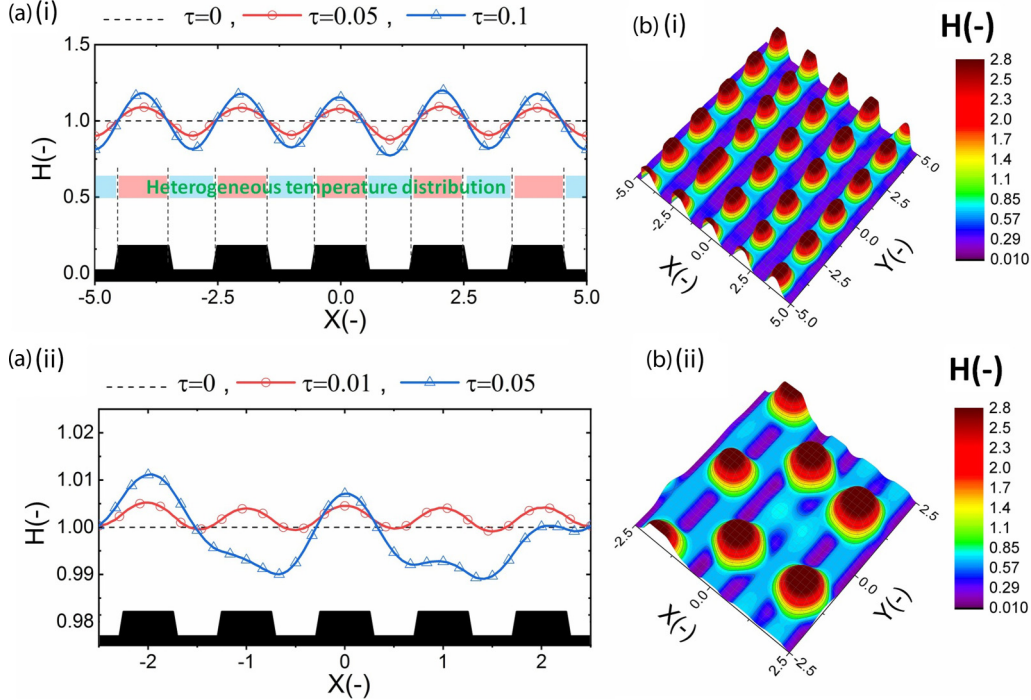
FIG. 10. Patterned lower plate (PLP) and AP model, interface height profile at (a) early stages of deformation and (b) quasisteady stage of pattern formation. Protrusion height $l_p = 0.1d$ and protrusion width $p_w =$ (i) $\lambda_{\max}$ and (ii) $0.5\lambda_{\max}$, initial film thickness, $h_0 = 35$ nm, and plates distance, $d = 100$ nm.

neighboring areas. When $p_w = \lambda_{\max}$ and t is small, interfacial deformations developed adjacent to both regions of heating and cooling [see Fig. 9(a)(i)]. Over time, the TC force became more dominant at valleys (areas with no protrusions, $l_p = 0$) and the first set of pillars formed there. Later, a second set of pillars formed above the ridges. These are smaller compared to those pillars formed initially [see Fig. 9(b)(i)]. The secondary pattern formation can be avoided by using smaller ridges and by lowering their periodicity to $0.5\lambda_{\max}$ [see Figs. 9(a)(ii) and 9(b)(ii)]. In contrast to the $p_w = \lambda_{\max}$ case, here only one set of pillars formed between adjacent ridges. The pillars so formed are aligned parallel to the ridges and have similar shape and size.

The spatiotemporal evolution of the interface under nonuniform heating conditions using a PLP and the AP model is shown in Fig. 10. One main difference with Fig. 9 is that the interface deformation is dominant above the ridges such that pillars formed only at these ridges [see Figs. 10(a)(i) and 10(b)(i)]. Lowering the ridge width from $p_w = \lambda_{\max}$ to $0.5\lambda_{\max}$ changed the dynamics as the initial deformations ($\tau = 0.01$) become distorted soon thereafter ($\tau = 0.05$) leading to a pattern where the pillars are larger and unevenly distributed [see Fig. 10(b)(ii)]. In this case, the introduction of temperature nonuniformities failed to create a well-ordered structures.

IV. CONCLUSIONS

Thermally induced interfacial instabilities and pattern formation in confined thin liquid films has been investigated. While the majority of previous efforts are limited to finding the corresponding mechanism for the growth of instabilities based on the initial stages of pattern formation, here we consider the nonlinear stages by way of numerical simulation of the relevant governing equations. Moreover, the commonly used uniform applied thermal gradient is replaced with laterally variable thermal gradient by introducing nonuniform cooling using a patterned top plate (PTP) and nonuniform heating using a patterned lower plate (PLP). Both linear and nonlinear stages of film evolution are compared for the acoustic phonon (AP) and thermocapillary (TC) models. Through this process, we estimate the threshold film thickness for the transition from pillar shapes to bicontinuous structures. Results are expressed in terms of the parameter D defined as the ratio of the plate separation distance to the initial (uniform) film thickness. A threshold value of $D \approx 2.5$ was obtained for both the TC and AP models. However, pattern formation is a highly transient process suggesting that a rapid quenching of the system to freeze structures in a particular geometric configuration will be successful only if sufficient time is allowed to elapse so that a quasisteady regime is realized. The number of created pillars in a $1\,\mu m^2$ domain is used to define pillar density, ρ_{pillar}. Increasing D leads to stable pillar formation and smaller features based on the TC model predictions, but for the AP model larger pillars as D increases is predicted.

In order to impose a nonuniform thermal gradient, patterned plates were used either as the top bounding plate (nonuniform cooling) or as the bottom bounding plate (nonuniform heating). The pattern sizes were adjusted based on the LS analysis predictions germane to each of the AP and TC models. In case of a PTP, both the TC and AP models showed that the deformation is dominant under the ridges. Considering the TC model as a reasonable descriptor

for interfacial deformations and using ridges with $p_w = \lambda_{\max}$ leads to two arrays of pillars under each ridge, whereas the AP model predicts only a single array of pillars. To achieve a well-organized nanoscale pattern, the TC model predictions suggest a ridge width of $0.5\lambda_{\max}$, whereas the AP model suggests that a ridge width of $\lambda_{\max}$ is more appropriate. In case of using a PLP, the mechanism of deformation is found to be different between the TC and AP models. In the former, the primary patterns form above the valleys, whereas in the latter they are formed above the ridges. Adjusting the protrusion width from $\lambda_{\max}$ to $0.5\lambda_{\max}$ enhanced the patterning in the TC model by inhibiting secondary pattern formation. However, in the AP model it results in larger pillars that are unevenly distributed.

APPENDIX: DERIVATION FOR DISPERSION RELATION IN LINEAR STABILITY ANALYSIS

In the linear stability analysis, the uniform interface height, H in Eq. (27), is superposed with a periodic perturbation such that $H = 1 + \xi \exp(\overline{\kappa}(X)\mathrm{i} + S(\overline{\kappa})\tau) + \mathrm{c.c.}$ where $\mathrm{i} = \sqrt{-1}$ and c.c. denotes the complex conjugate. Here we present the derivation leading to the dispersion relation in Eq. (31).

For thermally induced instabilities, the main deriving force leading to interface deformation is the TC (or AP) force. Hence, the contribution of intermolecular forces vis-à-vis instability growth and saturation is negligible, and Eq. (27) can be written as

$$\frac{\partial H}{\partial \tau} + \boldsymbol{\nabla} \cdot \left\{ \frac{H^3}{3} \mathrm{Ca}^{-1} \boldsymbol{\nabla}(\nabla^2 H) + \frac{H^2}{2} \frac{\mathrm{Ma}\,k_r D}{[(1 - k_r)H + k_r D]^2} \boldsymbol{\nabla} H \right\} = 0. \tag{A1}$$

Firstly spatial derivatives are expanded in the X direction (for the sake of simplicity, we here restrict attention to a purely 2D flow). Thus it can be shown that

$$\frac{\partial H}{\partial \tau} + \frac{\mathrm{Ca}^{-1}}{3} \left(3H^2 \underline{\frac{\partial H}{\partial X} \frac{\partial^3 H}{\partial X^3}} + H^3 \frac{\partial^4 H}{\partial X^4} \right) + H \underline{\left(\frac{\partial H}{\partial X}\right)^2} \frac{\mathrm{Ma}\,k_r D}{[(1 - k_r)H + k_r D]^2}$$

$$+ \frac{H^2}{2} \frac{\mathrm{Ma}\,k_r D}{[(1 - k_r)H + k_r D]^3} \left\{ \frac{\partial^2 H}{\partial X^2}[(1 - k_r)H + k_r D] - 2(1 - k_r)\underline{\left(\frac{\partial H}{\partial X}\right)^2} \right\} = 0. \tag{A2}$$

Nonlinear terms involving spatial derivatives (underlined) in Eq. (A2) are eliminated before considering a normal modes solution for H. Next, time and spatial derivatives (which appear in orders one, two, three, and four) in Eq. (A2) and power terms (H^2 and H^3) are substituted with the following expressions:

$$\frac{\partial H}{\partial \tau} = S(\overline{\kappa})\xi E, \quad \frac{\partial H}{\partial X} = \mathrm{i}\overline{\kappa}\xi E, \quad \frac{\partial^2 H}{\partial X^2} = -\overline{\kappa}^2 \xi E, \quad \frac{\partial^3 H}{\partial X^3} = -\mathrm{i}\overline{\kappa}^3 \xi E, \quad \frac{\partial^4 H}{\partial X^4} = \overline{\kappa}^4 \xi E,$$

$$H^2 = 1 + 2\xi E + (\xi E)^2, \quad H^3 = 1 + 3\xi E + 3(\xi E)^2 + (\xi E)^3, \tag{A3}$$

where $E = \exp[\overline{\kappa} X \mathrm{i} + S(\overline{\kappa})\tau]$ has been introduced as a notational shorthand. After expanding all terms and neglecting further nonlinear terms (ξ^2 and $\xi^3 \ll 1$), the following dispersion relation is obtained:

$$S(\overline{\kappa}) + \frac{\overline{\kappa}^4}{\mathrm{Ca}} - \frac{3\mathrm{Ma}\,k_r D}{2[(1 - k_r) + k_r D]^2}\overline{\kappa}^2 = 0. \tag{A4}$$

[1] X.-M. Zhao, Y. Xia, and G. M. Whitesides, J. Mater. Chem. **7**, 1069 (1997).

[2] S. R. Quake and A. Scherer, Science **290**, 1536 (2000).

[3] M. J. Madou, in *Fundamentals of Microfabrication: The Science of Miniaturization*, 2nd ed., edited by K. Ranjit (CRC Press, Boca Raton, 2002), pp. 1–72.

[4] B. D. Gates, Q. Xu, M. Stewart, D. Ryan, C. G. Willson, and G. M. Whitesides, Chem. Rev. **105**, 1171 (2005).

[5] E. Albisetti, D. Petti, M. Pancaldi, M. Madami, S. Tacchi, J. Curtis, W. P. King, A. Papp, G. Csaba, W. Porod, P. Vavassori, E. Riedo, and R. Bertacco, Nat. Nanotechnol. **11**, 545 (2016).

[6] J. P. Singer, J. Polym. Sci., Part B **55**, 1649 (2017).

[7] E. Schaffer, S. Harkema, M. Roerdink, R. Blossey, and U. Steiner, Adv. Mater. **15**, 514 (2003).

[8] S. Y. Chou and L. Zhuang, J. Vac. Sci. Technol. B **17**, 3197 (1999).

[9] N. Wu and W. B. Russel, Nano Today **4**, 180 (2009).

[10] H. Nazaripoor, C. R. Koch, and M. Sadrzadeh, J. Colloid Interface Sci. **530**, 312 (2018).

[11] R. Mukherjee and A. Sharma, Soft Matter **11**, 8717 (2015).

[12] H. Nazaripoor, C. R. Koch, M. Sadrzadeh, and S. Bhattacharjee, Langmuir **32**, 5776 (2016).

[13] H. Hu, H. Tian, J. Shao, Y. Ding, C. Jiang, and H. Liu, J. Micromech. Microeng. **24**, 095027 (2014).

[14] S. H. Davis, Annu. Rev. Fluid Mech. **19**, 403 (1987).

[15] M. Dietzel and S. M. Troian, Phys. Rev. Lett. **103**, 074501 (2009).

[16] M. Dietzel and S. M. Troian, J. Appl. Phys. **108**, 074308 (2010).

[17] H. Nazaripoor, C. R. Koch, M. Sadrzadeh, and S. Bhattacharjee, Soft Matter **12**, 1074 (2016).

[18] A. Sharma and R. Khanna, Phys. Rev. Lett. **81**, 3463 (1998).

[19] E. McLeod, Y. Liu, and S. M. Troian, Phys. Rev. Lett. **106**, 175501 (2011).

[20] F. Ay, A. Kocabas, C. Kocabas, A. Aydinli, and S. Agan, J. Appl. Phys. **96**, 7147 (2004).

[21] K. R. Fiedler and S. M. Troian, J. Appl. Phys. **120**, 205303 (2016).

[22] T. R. Kotni, R. Khanna, and J. Sarkar, J. Phys.: Condens. Matter **29**, 175001 (2017).

[23] R. W. Atherton and G. M. Homsy, Chem. Eng. Commun. **2**, 57 (1976).

[24] M. B. Williams and S. H. Davis, J. Colloid Interface Sci. **90**, 220 (1982).

[25] J. N. Israelachvili, *Intermolecular and Surface Forces* (Academic Press, Burlington, MA, 2011).

[26] C. Albanese, P. Dell'Aversana, and F. S. Gaeta, Phys. Rev. Lett. **79**, 4151 (1997).

[27] E. Schäffer, S. Harkema, R. Blossey, E. U. Steiner Schaffer, S. Harkema, R. Blossey, and U. Steiner, Europhys. Lett. **60**, 255 (2002).

[28] E. Schäffer, S. Harkema, M. Roerdink, R. Blossey, and U. Steiner, Macromolecules **36**, 1645 (2003).

[29] T. Gambaryan-Roisman, Adv. Colloid Interface Sci. **222**, 319 (2015).

[30] W. H. Vandevender and K. H. Haskell, Signum Newsletter **17**, 16 (1982).

[31] L. R. Petzold, *Proceedings of the IMACS World Congress, Montreal, Canada* (1982).

[32] K. E. Brenan and L. R. Petzold, SIAM J. Numer. Anal. **26**, 976 (1989).

[33] K. E. Brenan, S. L. Campbell, and L. R. Petzold, in *Numerical Solution of Initial-Value Problems in Differential-Algebraic Equations*, edited by R. E. O'Malley, Jr. (SIAM, Philadelphia, 1996), pp. 15–39.

[34] R. S. Maier, L. R. Petzold, and W. Rath, in *Proceedings of the Scalable Parallel Libraries Conference* (IEEE, Mississippi State, 1993), pp. 174–182.

[35] H. Nazaripoor, Ph.D. thesis, University of Alberta (2016).

[36] N. Wu, M. E. Kavousanakis, and W. B. Russel, Phys. Rev. E **81**, 026306 (2010).